

Reaction-free concentration gradient generation in spatially non-uniform AC electric fields

Ran An¹, Adrienne R. Minerick^{1*}

¹Department of Chemical Engineering, Michigan Technological University, Houghton, MI, USA, 49931

Abstract

The ability to generate stable, spatiotemporally controllable concentration gradients is critical for both electrokinetic and biological applications such as directional wetting and chemotaxis. Electrochemical techniques for generating solution and surface gradients display benefits such as simplicity, controllability, and compatibility with automation. Here, we present an exploratory study for generating micro-scale spatiotemporally controllable gradients using a reaction-free electrokinetic technique in a microfluidic environment. Methanol solutions with ionic Fluorescein isothiocyanate (FITC) molecules were used as an illustrative electrolyte. Spatially non-uniform alternating current (AC) electric fields were applied using hafnium dioxide (HfO₂) coated Ti/Au electrode pairs. Results from spatial and temporal analysis, along with control experiments suggest that the FITC ion concentration gradient in bulk fluid (over 50 μm from the electrode) was established due to spatial variation of electric field density, and was independent of electrochemical reactions at the electrode surface. The established ion concentration gradients depended on both amplitudes and the frequencies of the oscillating AC electric field. Overall, this work reports a novel approach for generating stable and spatiotemporally tunable gradients in a microfluidic chamber using a reaction-free electrochemical methodology.

Keywords: Microdevice, Non-uniform AC electric fields, Chemical Gradient, Electrochemistry

Total Words: 5258

Abbreviations: Gradient generation, Fluorescein isothiocyanate (FITC), Hafnium Oxide (HfO₂), Electrophoresis (EP)

*To whom correspondence should be addressed: minerick@mtu.edu, 1400 Townsend Drive, 203 Chemical Sciences and Engineering, Houghton, MI 49931

1. Introduction

Spatial and temporal gradients are essential both in solution and on surfaces of many systems and applications [1-6]. In biological systems, gradients play important roles in cell signaling, migration, differentiation, and metastasis [7-11]. In electrokinetic relevant applications, gradients are utilized for high-throughput material screening and to steer molecular motion, among others [4, 12, 13].

Conventional gradient-generation platforms are based predominantly on diffusion, printing, dip coating, or irradiation [14]. These techniques, however, only produce static, monotonic gradients that have fixed physiochemical properties, whereas studying dynamic biomolecular responses and controlling molecular motion both require spatially and temporally controllable gradients [15].

Microfluidic platforms have been used to generate chemical gradients which feature spatial and temporal control [16-18]. However, the majority of microfluidic-based gradient generation systems employ passive mixing or free-diffusion[17], resulting in gradients with limited spatiotemporal resolution[16]. In contrast to passive generation of concentration gradients, electrochemical techniques actively create dynamic surface gradients that feature compelling controllability and flexibility [19]. Additionally, electrochemical gradient generation techniques are highly versatile, are compatible with organic and inorganic systems, can be integrated with electronics, and are easily automated [19].

The fundamental theory for electrochemical concentration gradient generators are based on ion mass transfer, which can be described by the combination (3) of the Nernst-Planck (1) and mass-conservation (2) equations [20].

$$\vec{J}_i = -D_i \vec{\nabla} C_i - \frac{z_i F}{RT} D_i C_i \vec{\nabla} \phi + C_i \vec{v} \quad (1)$$

$$\frac{\partial C_i}{\partial t} + \vec{\nabla} \cdot \vec{J}_i + R_i = 0 \quad (2)$$

$$\frac{\partial C_i}{\partial t} = D_i \vec{\nabla}^2 C_i + \frac{z_i F}{RT} D_i C_i \vec{\nabla}^2 \phi - C_i \vec{v} + R_i \quad (3)$$

where \vec{J}_i , D_i , C_i and z_i are the flux (vector), diffusion coefficient, concentration, and valence of species i , respectively. R is the gas constant, T is temperature, F is Faraday's constant, ϕ is electric potential, \vec{v} is convective flow velocity (vector), t is time, and R_i is the reaction rate for species i . From Eqn (3), the time dependence of ion concentration for species i within a fluid can be induced by chemical potential gradients, electric potential gradients, convective flows, and species i reactions. Such reactions can be ionic, chemical, and/or Faradaic in nature.

Current electrochemical gradient generation approaches are based on mass transfer induced by Faradaic reactions [21], gradients derived from in-plane potential gradients [22], bipolar electrochemical gradients [23], gradients produced using an asymmetric electrode configuration [24], as well as combinations of electrochemistry with other methods such as photomask [25], dip coating [26], and magnetic field [27]. Many of these approaches rely on Faradaic reactions (R_i) that yield species accumulation for gradient generation.

According to Eqn 3, we hypothesized that stable concentration gradients, $\vec{\nabla}^2 C_i$, can be generated using biased electromigration in spatially non-uniform alternating-current (AC) electric fields ($\frac{z_i F}{RT} D_i C_i \vec{\nabla}^2 \phi \neq 0$), independently from bulk flux ($C_i \vec{v} = \mathbf{0}$) and without Faradaic reactions ($R_i = 0$). To test our hypothesis, ionized fluorescent dye Fluorescein isothiocyanate (FITC), was used as a real-time detectable target. To suppress the dominant Faradaic reaction manifesting as water electrolysis, 1) methanol (MeOH) was used as a solvent instead of water [28], and 2) a dielectric layer of hafnium dioxide (HfO_2) was implemented over the Ti/Au electrode to block the electron exchange between the electrode metal surface to any residual water molecules [29].

In this work, we first performed qualitative control experiments to ascertain impacts on spatiotemporal fluorescent emission intensity from Faradaic reactions as well as convective flow (per mechanisms in eqn 3). This ensured the fluorescent emission intensity changes detected in the remaining experiments could be decoupled and attributable to electromigration mechanisms. Then, we performed spatial and temporal analysis on the intensity behavior and

visually tabulated the ion concentration gradients using contour plots. Finally, we quantified ion concentration gradients as a function of applied potential from 5 to 10 V_{pp} and frequencies from 5- to 25-times the electrode charging frequency f_c , defined in Eqn 4.

2. Materials and Methods

2.1. Materials

Fluorescein isothiocyanate (FITC, 492/518 nm) was utilized as a fluorescing ion source. FITC (powder $\geq 90\%$, Sigma-Aldrich, USA) stock solution was prepared in MeOH (99.99%, Sigma-Aldrich, USA) at 10^{-4} M and further diluted to 2 μ M during experiments. Rhodamine B (Rb, powder $\geq 95\%$, 554/627 nm, Sigma-Aldrich, USA) was utilized as a neutral dye in control experiments. Rb stock solution was also prepared in MeOH at 10^{-4} M further diluted to 2 μ M during experiments. NaCl ($>99\%$, Macron Chemicals, USA) was used in the MeOH solution during the Rb control experiment to provide the same solution conductivity (4.3×10^{-4} S/m) as the 2 μ M FITC solution.

2.2. Microdevice Design and Fabrication

Orthogonally positioned Ti/Au (50/50 nm thickness, 100 μ m width) electrode pairs with 100 μ m gaps were designed and fabricated following standard soft photolithography fabrication procedures on microscope slides [30]. Additionally, a layer of 100 nm hafnium dioxide (HfO₂) was sputter coated over the entire glass slide to provide a physical dielectric barrier above the electrode [29]. Fig. 1 shows a) photo of the fully assembled microdevice, b) 10x magnified view of the experimental fluidic chamber, and c) side view schematic of the device illustrating the dielectric HfO₂ layer. An Agilent 33250A function generator provided the AC electric signal across the vertical electrode, $V_{pp}\sin(\omega t)$, and grounded horizontal electrode to drive ion migration within the chamber.

2.3. Experiments

Two approaches were employed to significantly reduce Faradaic reactions at the electrodes. The first approach employed a dielectric coating hafnium dioxide (HfO₂) [29, 31] previously

demonstrated to provide a physical and insulating dielectric layer between the Ti/Au electrodes and the electrolyte while still enabling electric potential penetration into the solvent. The electrical current through the solution, while attenuated slightly by the HfO₂, remained sufficient to induce ion migration within the experimental conditions explored [32]. The second approach utilized MeOH as an electrochemically inert solvent in place of water. MeOH has been shown to better resist electrolysis [33].

After independently developing concentration/intensity calibration curves, FITC and Rb photobleaching were also quantified separately by continuously detecting emission light intensity in the working chamber under excitation light exposure for 60 s and in the absence of an applied electric potential.

Solutions were prepared by mixing prepared FITC stock solution and MeOH at the ratio of 1:49 yielding a final FITC concentration of 2 μ M for the ion migration detection experiments. Samples were injected into the input port shown in Fig. 1(a) and sealed with a one-piece fitting (LabSmith, USA). This batch experiment prevented pressure driven flow within the chamber (separately verified). The experimental matrix included AC signals from 5 to 10 V_{pp} at 1.25 V_{pp} intervals and frequencies from 100 to 500 Hz at 100 Hz intervals; this corresponded to 5-25 times f_c (eqn 4).

To facilitate comparison of study results for other systems with various electrode designs and solutions, we utilized a non-dimensional frequency which was obtained by dividing the applied frequency with the electrode charging frequency, f_c . The electrode charging frequency captures the propensity of the electric double layer to charge according to the following equation [34]:

$$f_c = \frac{1}{2\pi t_c} = \frac{D}{2\pi \lambda_D L} \quad (4)$$

$$\lambda_D = \sqrt{\frac{\epsilon RT}{2F^2 C_0}} \quad (5)$$

$$f_r = \frac{f}{f_c} \quad (6)$$

Where, f_c is electrode charging frequency, D is diffusion coefficient, λ_D is electrical double

layer thickness, L is characteristic length (in this case the 100 μm spacing between electrodes), ϵ is solution relative permittivity, C_0 is bulk molar concentration, f is applied frequency, and f_r is relative frequency. Under the experimental conditions of this work, $D = 4.9 \times 10^{-10} \text{ m}^2/\text{s}$ for FITC in methanol for FITC in methanol, which was roughly estimated via linear proportional analysis of the diffusion coefficient of FITC in water [35, 36] to the diffusion coefficient of sodium in water and in methanol [37]. The electrode charging frequency was calculated to be ~ 20 Hz using parameters above and $\epsilon = 33$ for FITC in MeOH [38]. Thus, the applied non-dimensional relative frequency, f_r , ranged from 5 to 25. Video microscopy at 10x magnification was recorded at 1 fps for 60 seconds. No electric fields were applied in the first 5 frames to check system stability. Each 60 s experiment was repeated 5 times with new solutions in the microchamber.

Control experiments were completed to detect convective flow using a mixture of neutrally charged 2 μM Rb dye in NaCl MeOH solution with NaCl added to achieve $4.3 \times 10^{-4} \frac{\text{S}}{\text{m}}$. This was the same final conductivity as the FITC-MeOH solution. Additional control experiments were completed to detect Faradaic reaction by-products (i.e., pH changes) using 2 μM FITC-MeOH solution within uniform electric field without the HfO_2 layer as described in our previous work [39].

In addition, the COMSOL Multiphysics[®] (COMSOL, Inc, Burlington, MA) electrostatics module was used to simulate electric field spatiotemporal variations including field strengths and field densities within the inspected system (Extra Fine mesh). As illustrated in Figure 1, the horizontal electrode at the top of the simulated region was set to a ground condition. The vertical electrode was fixed to 10 V_{pp}, the left and right boundaries were configured as open, and the remaining boundaries were programmed as insulating.

2.4. Data Analysis Methods

Emission intensities of FITC and Rb dyes were tested independently against time for the effect of photobleaching (Fig. 2a&b), and against fixed FITC and Rb concentrations for obtaining

each intensity-concentration calibration curve (Fig. 2c&d).

All acquired microscope videos were exported as 61 (0-60 s) separate images and imported into MATLAB to generate grayscale matrixes ranging from 0 (dark) to 255 (bright). Intensity values of the first 5 frames (electric fields off) were normalized to 75 to ensure the brightest regions did not exceed the 255 maximum range.

For control experiments, intensity analysis was performed on the acquired video to calibrating for photobleaching (Fig. 2a&b). For test experiments, the acquired data were calibrated against photobleaching effects (Fig. 2a&b), then converted to FITC concentration using to the FITC calibration curve (Fig. 2c).

Contour 3-D mesh image plots were used to aid in visualizing the ion concentration gradient. Contour plots were used to demonstrate the intensity spatiotemporally to discern gradient progression and 3-D mesh images were used to demonstrate the calculated concentration gradient whereby the z-axis expresses FITC concentration obtained from the FITC concentration-intensity calibration.

Image J was employed to quantify peak-to-peak potential and frequency dependencies. An area of interest (area F in Fig. 5, total area $\sim 35,000 \mu\text{m}^2$) was chosen in the high field density region. Additional areas of interest (areas A-E in Fig. 5, total areas $\sim 15,000 \mu\text{m}^2$, $30,000 \mu\text{m}^2$, $105,000 \mu\text{m}^2$, $47,000 \mu\text{m}^2$, and $45,000 \mu\text{m}^2$) were ascertained based on visually uniform intensity over the area. These areas of interest were then used to track emission intensity over time and quantify concentration temporally.

3. Results and Discussion

The FITC anion was selected to measure spatially variant ion concentration in a non-ionic MeOH solution; it is a fluorescing molecule whose concentration is directly proportional to emission intensity. FITC and Rb were first calibrated to quantify photobleaching effects and to obtain emission intensity versus concentration calibration curves. Control experiments were performed utilizing FITC and Rb to ascertain extent of Faradaic reactions in two modified

devices (non-uniform and uniform) and to determine effects from convective flow. Spatial emission intensity analysis was performed in the spatially variant electric fields followed by time analysis of ion concentration changes in multiple areas. Finally, ion gradient dependencies on applied potential magnitudes and frequency were quantified.

3.1. FITC and Rb Calibrations

FITC and Rb calibrations were completed to quantify both photobleaching and intensity-concentration correlations. Photobleaching properties were examined by detecting FITC (Fig.2a) and Rb (Fig.2b) emission intensity without applying any potential for 60 s. Results showed that FITC emission intensity decreased from 75 arb. unit to 55 while Rb emission intensity stayed nearly constant at 75 during the entire 60 s. FITC photobleaching can be fit to an exponential function and Rb photobleaching can be fit to a linear function, both with $R^2 > 0.99$. These functions were used to correct subsequent experiments to isolate photobleaching effects and obtain net intensity change from dye concentration changes only.

Second, both FITC and Rb concentrations were calibrated with emission intensity as shown in Fig. 2(c & d, $n = 3$). Both FITC and Rb emission intensity increased with dye concentration from 2 μM to 12 μM . Polynomial equations were fit with $R^2 > 0.99$. Once experiments were conducted in electric fields, FITC intensity was corrected to isolate concentration-only effects by using the calibration curves in Fig. 2(a & c). Similarly, Rb intensity was corrected to isolate concentration using the calibration curves in Fig. 2(b & d).

3.2. Control Experiments

Four sets of control experiments were conducted to elucidate other mechanisms that could potentially impact FITC emission intensity changes. Mechanisms in the Nernst-Planck equation (1) including diffusion, reaction, convection, and electromigration impact ion concentrations over time. Diffusion is a passive process that exists in all systems at around 10 $\mu\text{m}^2/\text{s}$ for FITC molecules [40]. More specifically, diffusivity of FITC $D = 4.9 \times 10^{-10} \text{ m}^2/\text{s}$ yields a diffusion time of $t \approx \frac{x^2}{2D} = 10 \text{ s}$ to travel the x distance of 100 μm , which is 10^3 times longer

than the period of the AC signal (100 Hz, 0.1 s). Faradaic reactions occur due to charge transfer at electrode surfaces; these effects need to be examined since reaction byproducts have been shown to affect pH adjacent to the electrodes [41, 42] and thus FITC dye emission intensity. For convective flow, AC electroosmotic flow could potentially be induced at the frequencies and conductivities examined [43]. Such induced flows would transport dye thus affecting observed emission intensities. Electromigration could not be controlled and was therefore intentionally quantified including comparisons between the ion intensity changes in uniform and non-uniform devices.

10 V_{pp} at 100 Hz sinusoidal signals were applied on all four sets of control experiments including neutral Rb dye in uniform electric fields (Fig. 3, 1st column), ionic FITC dye in uniform electric fields (Fig. 3, 2nd column), ionic FITC dye in non-uniform electric fields (Fig. 3, 3rd column), and neutral Rb dye in non-uniform electric fields (Fig. 3, 4th column). Captured data at 0 s, 7 s (2 s after applying electric fields), and 60 s are shown in row 1 to row 3 Fig. 3(a-d), 3(e-h), and 3(i-l), respectively. Fig. 3(m-p) demonstrates the absolute difference between 60 s and 0 s to better visualize intensity change over the experiment.

In the first column, Rb-NaCl MeOH solution in a uniform electric field demonstrated nearly constant emission intensity Fig. 3(a, e, i, m). Since Rb has also been utilized as a temperature indicator [44], this result indicates that there is no significant temperature change, which is expected given the low conductivity of the solution. The estimated temperature change would be ~0.01 °C according to $\Delta T = \frac{\sigma V_{rms}^2}{8k}$, where $\sigma = 0.00043 \text{ S/m}$ is the solution conductivity and thermal conductivity, $k=0.203$, for MeOH at 25 °C. Experiments and theory are in agreement; the experimental conditions in this system are thermally stable.

To qualify ion concentration change induced by Faradaic reactions ($\frac{\partial C_i}{\partial t}$ induced by R_i), FITC MeOH solution at a conductivity of $4.3 \times 10^{-4} \text{ S/m}$ was monitored between a pair of parallel electrodes whereby the electric field gradient is nearly zero, $\nabla^2 \phi = 0$ (Fig. 3, 2nd row). Uniform AC electric fields yield zero time-averaged ion migration, $\left[\frac{z_i F}{RT} D_i C_i \vec{\nabla} \phi \right] = 0$, as well as zero

convective flow, $C_i \vec{v} = 0$, while Faradaic reactions remain present, $R_i \neq 0$. As a result, all observed intensity shifts (ΔI) in uniform fields can be attributed to Faradaic reactions. FITC emissions in the uniform electric field remained nearly constant as illustrated in the second column in Fig. 3(b, f, j). A small decrease in intensity was observed in Fig. 3(n) and calculated over all repeats to have an average magnitude of 7.5 arb. unit. This was attributed to residual Faradaic reactions progressing with the aid of water contamination in MeOH [45] via any HfO_2 pits or exposed edges of the Au electrode that can be exposed during the photoresist lift-off process [46]. While Faradaic reactions do not depend on field uniformities, they do cause shifts in pH that alter FITC intensity; these minor effects are a form of systematic error and are quantifiable from the uniform field experiments. However, Fig. 3(n) demonstrates that these residual Faradaic reaction byproducts are so minor (7.5 arb. unit) that they can be decoupled from the mechanism inducing FITC concentration intensity increases in non-uniform electric fields, as shown in Fig. 3(c, g, k, and o). Our group systematically characterized Faradaic reaction pH changes in a previous publication [39].

As shown in the fourth column of Fig. 3(d, h, l), controls were also conducted in uniform AC electric fields with the neutral Rb-NaCl solution whereby any observed intensity shift (ΔI) can be attributed to convective flow. The magnitude of intensity change demonstrated in Fig. 3(p) was ~ 0 . Since the Rb-NaCl and FITC solutions have identical conductivities, any induced ACEO flow would have been similar (eqn 3 in [43]). The imperceptible Rb intensity change in Fig. 3(p) indicates ACEO flow was not induced under these ionic conditions in this system. Thus, convective flow is not the mechanism inducing the observed FITC emission intensity increases in non-uniform electric fields.

The third column in Fig. 3 illustrates FITC in MeOH in the non-uniform electric field. Prior to electric field application, the system initially displays a uniform intensity as shown in Fig. 3(c). The emission intensity starts to increase from the high field density region after 2 s within the electric field as shown in Fig. 3(g). In Fig. 3(k) and Fig. 3(o), significant intensity increases were quantified with average magnitude of 120 arb. units in the gap between the electrodes at

a longer time of 60 s and a longer length scale of $\sim 100 \mu\text{m}$.

In conclusion, these control and comparison experiments illustrate that the observed FITC intensity changes in Fig. 3(c, g, h and o) are not induced by temperature changes, Faradaic reactions, or convection. Per the N-P mass conservation eqn (3), electromigration is the remaining ion transport mechanism.

3.3. Proposed Mechanism for the Established Ion Concentration Gradient

Mechanisms for ion motion over time in non-uniform alternating-current electric fields have remained somewhat ambiguous because ion migrations in bulk solution under AC fields are traditionally assumed to be negligible [47]. However, theories and supporting evidence have been advanced that ions experience oscillatory migration in AC fields resulting in accumulating solution property changes over time [48].

In this work, we hypothesized that a stable concentration gradient, $\vec{\nabla}^2 C_i$, can be generated leveraging the mechanism of biased electromigration in spatially non-uniform AC electric fields ($\frac{z_i F}{RT} D_i C_i \vec{\nabla}^2 \phi \neq 0$), independently from bulk convective flow ($C_i \vec{v} = \mathbf{0}$) and Faradaic reactions ($R_i = 0$).

At quasi-equilibrium, whereby the total number of ions within the chamber do not change, the time averaged ion concentration variation with time is zero $\frac{\partial C_i}{\partial t} = \mathbf{0}$. In this quasi-equilibrium state, the Nernst-Planck equation (Eqn. 3) then indicates that the spatial ion concentration gradient, $D_i \vec{\nabla}^2 C_i$, is associated with convection, $-C_i \vec{v}$, reactions (in this case, Faradaic reactions), R_i , and electric field gradient, $\frac{z_i F}{RT} D_i C_i \vec{\nabla}^2 \phi$. Results obtained from the control experiments (Fig. 3) indicate that effects from convective flow and Faradaic reactions are nearly negligible, thus $C_i \vec{v} = 0$, $R_i = 0$. As a result, the simplified N-P conservation equation (Eqn. 3) describing the experimental conditions can be simplified to:

$$-D_i \vec{\nabla}^2 C_i = \frac{z_i F}{RT} D_i C_i \vec{\nabla}^2 \phi \quad (7)$$

Equation 7 indicates that the intensity change observed in the FITC-MeOH solution in non-

uniform electric field is predominantly induced by electromigration, $\frac{z_i F}{RT} D_i C_i \vec{\nabla}^2 \phi$, leading to a stable establishment of an ion concentration gradient, $\vec{\nabla}^2 C_i$, within the microfluidic chamber.

Thus, our hypothesis agrees with the experimental results from comparative control experiments. When $\vec{\nabla}^2 \phi = 0$ in uniform electric fields, no ion concentration gradient is established. On the contrary, in non-uniform electric fields, $\vec{\nabla}^2 \phi \neq 0$, the non-zero gradient of the electric field shown is responsible for inducing an ion concentration gradient. The similar pattern between the experimentally established ion concentration gradient and the electric field gradient calculated from $\vec{\nabla}^2 \phi$ also supports this hypothesis. Fig. 4 shows comparison between the contour plot for emission intensity (Fig. 4 a,b) of the FITC concentration distribution at $t=7$, and 30 s alongside the electric field density simulated by Poisson's equation in COMSOL's electrostatics module (Fig 4 c,d). For best visualization, Fig. 4(c) shows the field density on a scale from 1×10^9 to 5×10^9 V/m² while Fig. 4(d) shows data in the scale from 4×10^8 to 2×10^9 V/m². Rough similarities are visible in Fig. 4(a) and (c) whereby FITC ion concentrations enrich from the highest field density area at the corners of the point electrode in the chamber and progress to dominate the narrow gap between the electrodes. As time progresses, ion enrichment increases and the enrichment area expands down the electric field gradient with lower concentrations in the peripheral areas.

Pattern variations on either side of the vertical electrode when comparing between Fig. 4(b) and (d) are attributed to minor pH induced intensity changes [49] and diffusion. pH changes from residual Faradaic reactions could occur at exposed Ti/Au electrode pits or edges as discussed in section 3.2. Patterns of more severe ion shifts around a high field density electrode tip were previously observed [50]. In addition, impacts from diffusion, while >100 orders of magnitude less than migration, may also contribute to the slight differences in shape between the actively generated ion concentration gradient and electric field density. Since the lower left and right sides are microfluidic channels (Figs. 1b and 5m) connected with buffer reservoirs (Fig. 1a), these are functioning as boundaries with constant concentration. As a result, ion diffusion can

be occurred in this limited cross section between the bulk fluid area (i.e., area C in Fig. 5m) and the microchannels.

In summary, while slight variations exist between the spatial patterns in electric field gradient simulations and experimentally-measured ion concentrations, the generated FITC concentration gradient within a 680 μm by 900 μm chamber is directly dependent upon the existence of spatial non-uniformity in an applied AC electric field.

3.4. Temporal and Spatial Analysis of Intensity Change

Additional temporal and spatial analyses were performed to further characterize the FITC concentration gradient within the microchamber. Fig.5 demonstrates experimental results at 10 V_{pp} and 100 Hz in 4.3×10^{-4} S/m and 2 μM FITC solution. Each individual image includes the average FITC concentration out of 5 repeated tests. The photobleaching-corrected data was then fit to the calibration curve shown in Fig. 2(c) to obtain FITC concentrations as shown in the second row of Fig 5 (e, f, g, h). Results are organized into columns corresponding to experiment time: column 1 (a, e, i) shows results at $t=0$, column 2 (b, f, j) shows results at $t=7$ s (2 s after applied electric field), column 3 (c, g, k) shows results at $t=30$ s and column 4 (d, h, l) shows results at $t=60$ s. Different rows demonstrate results obtained by different image analysis methods: the first row shows 2-D grayscale intensity image (a-d), the second and third rows show FITC concentration in 3-D mesh images where the z axis demonstrates FITC concentration (e-h), and contour plots all generated by MATLAB. Fig. 5(m) shows the areas from which averaged FITC concentration was obtained using ImageJ. The areas were chosen according to the contour plot shown in Fig. 5(l). Area A shows the highest emission intensity thus highest FITC concentration during the entire experiment. Area B is the area surrounding the tip of the vertical electrode. Area C is the bulk solution area, where FITC concentration stayed relatively constant. Area D and E are corner areas where lower emission intensity was attributed to FITC concentration depletion. Areas B, C, D and E are all symmetric around the vertical electrode indicated by the white dashed line of symmetry. The inset in Fig. 5(m) shows the interest area F, where the electric field density was strongest representing greatest AC

electrokinetic phenomena. The area G represents the entire chamber. Fig. 5(n) shows the average FITC concentration for each specific area as a function of time.

At $t=0$ (first column) when no electric field was applied, Fig. 5(a,e,i) demonstrate uniform intensity; for subsequent analysis, this initial intensity is always normalized to 75 arb. unit to reference experiment to experiment comparisons (see section 2.4). Fig. 5n reflects this flat concentration in all regions for the first 4.9 seconds. These plots demonstrate the uniform FITC concentration distribution in the microdevice system when the system is free of impact from a non-uniform electric field.

At $t=7$ s (second column), 2 s after applying the electric field, Fig. 5 (b,f,j) demonstrate that FITC concentration increased to ~ 6 μM in area A, remained constant in areas B and C, and decreased slightly in corner areas D and E. Another observation is that the pattern of FITC concentration enrichment over the first two seconds matches closely with the electric field density distribution shown in Fig.4(c), consistent with the electromigration mechanism discussed prior.

The first 2 s correspond to the first 200 cycles of alternating current oscillation and demonstrate a net enrichment of FITC ions into the high electric field density areas near the electrode and depletion from corner regions farthest from electrodes. Since enrichment is dominated by electromigration, the depletion can be attributed to mass conservation. FITC ions migrated from weakest electric field areas toward strongest electric field areas and there is insufficient time for diffusion from the side channels to replenish the depleted area. More specifically, diffusivity of FITC $D = 4.9 \times 10^{-10} \text{ m}^2/\text{s}$ yields a diffusion time of $t \approx \frac{x^2}{2D} = 10 \text{ s}$ to travel the x distance of 100 μm ; thus, FITC molecules have insufficient time to travel from the side channel to the chamber.

At $t=30$ s, peak FITC concentrations approaching 10 μM were detected in a subset of area A (Fig. 5 g and k). In peripheral areas B, moderate FITC concentrations around 4.5 μM were observed and the magnitude of enrichment decreased with increasing distance from the high

field density area (Fig. 5 g and k). From 30 s to 60 s, observed FITC concentrations demonstrated a collective relaxation over the entire area. The most rapid concentration decreases were observed in areas B and E (Fig. 5n), while FITC concentrations $<1\ \mu\text{M}$ were observed in corner areas D and E (Fig. 5 l and n). Importantly, FITC concentration in the entire imaged area (area G) remained largely unchanged consistent with the conservation of total FITC molecules within the system.

These spatiotemporal FITC concentration changes can be attributed to the combined effect of electromigration, residual Faradaic reactions, and diffusion with electromigration significantly dominating. At $t = 7\ \text{s}$, FITC ions experience strong biased electromigration and accumulation into three- to five-fold concentration increases in areas with the highest electric field density. From $t = 7\ \text{s}$ to $t = 30\ \text{s}$, the relatively strong biased electromigration induced FITC ion concentration increases in areas A and B with high electric field density, with a corresponding depletion of FITC ion in areas D and E with low electric field density consistent with the N-P conservation equation. The overall observed concentration decrease from 30 s to 60 s can be partially attributed to residual Faradaic reactions decreasing the environment pH and thus the FITC emission intensity as shown in the control experiment (Fig. 3n). FITC concentration remained relatively stable in area C which had low electric field density as well as a direct connection with inlet/outlet channels that act as sources of $2\ \mu\text{M}$ solution; thus, area C has the greatest propensity to illustrate a balanced effect between electromigration and diffusion.

In summary, area G illustrates conservation of FITC within the entire observed system while areas A and F showed significant FITC concentration increase and areas C, D, and E concentration decreases dominated by electromigration effects. From 30 to 60 s, FITC concentration stabilized as electromigration reached a quasi-equilibrium balance with diffusion. Residual Faradaic reactions probably contributed to the measured FITC emission intensity decrease, even if the ion concentration may not have actually decreased. Therefore, in the next section, frequency and peak-to-peak analyses were performed on FITC concentrations at $t=30\ \text{s}$ instead of at $t=60\ \text{s}$ to exclude effects from Faradaic reactions best isolate and analyze

electromigration.

3.5. Peak-to-peak Potential and Frequency Dependency

We further hypothesized that the concentration gradients generated could be easily controlled by changing peak-to-peak potential (V_{pp}) and frequency of the applied AC field. To test our hypothesis, potential and frequency dependency of FITC concentrations were examined from 5 V_{pp} to 10 V_{pp} at a fixed frequency of 100 Hz and from 100 Hz to 500 Hz (relative frequency=5 to 25) at a fixed applied potential of 10 V_{pp} . The minimum potential and frequency were determined according to the observed negligible intensity increase below 5 V_{pp} and above 500 Hz. The maximum potential and frequency were determined due to observed shorter device life at frequencies below 100 Hz and instrument maximum V_{pp} . Average intensity shifts in interest area F between $t=5$ s and 35 s were examined since the strongest indicators of electromigration were prominent between the electrodes in Fig. 5. Fig. 6(a & b) demonstrate the average FITC concentration from 5 repeat experiments for each potential/frequency condition, while standard deviations < 0.1 μ M demonstrate high reproducibility of this reported approach. Electrical potential dependency results indicate that the magnitude of FITC concentration increased with V_{pp} (Fig. 6a). The FITC concentration remained unchanged from the initial concentration of 2 μ M at 5 V_{pp} , but reached 4 μ M in a 10 V_{pp} field. This magnitude of enrichment with V_{pp} can be understood as higher applied potentials provided stronger electric fields causing ions to migrate further in each half cycle of the AC signal. As a result, the rate of establishment and magnitude of the FITC concentration gradient is greater at higher applied potentials.

Frequency dependency results indicate that the magnitude of FITC concentration decreased with frequency. However, FITC concentration gradients still existed at 400 Hz, a value 20 times higher than the electrode charging frequency. This decreased magnitude with increasing frequency agreed with a previous theoretical study by Golovnev et al. [51]. In their work, an analytical solution of the Poisson-Nernst-Planck (PNP) equation under applied AC potentials was reported and suggested that the change of ion concentrations with time was inversely related to frequencies of the applied signal. The physical mechanism of decreased FITC

concentration with frequency is probably due to the decreased available time for ion migration within each half cycle of the applied signal, which leads to attenuated concentration gradients.

4. Conclusions

Here, we demonstrated feasibility for a novel reaction-free approach for generating spatiotemporally controllable gradient within a batch microfluidic system. This approach is based on biased electromigration induced by spatially non-uniform AC electric fields. Control experiments were carefully designed and conducted illustrating electrothermal effects, diffusion, Faradaic reactions, and convection were minimal or negligible. Through strategic calibration and careful control, this body of experiments verified that the observed intensity changes were induced by electromigration-driven formation of an ion concentration gradient. The spatial and temporal properties of generated gradients were systematically characterized via the parametric dependence of two driving factors, peak-to-peak potential and frequency, on the FITC concentration gradient. Concentration gradients were generated within 10 s after applying the electric field and remained stable over the course of 60-second experiments. Results demonstrated up to a five-fold increase in maximum concentration above the initial concentration. Additionally, the magnitude of generated gradients can be accurately and reproducibly controlled via the applied peak-to-peak potential and frequency. Concentration gradients were shown to increase with increased potential and decrease with increased frequency of the applied AC fields. To the best of our knowledge, this is the first demonstration of a reaction-free approach for generating spatiotemporally controllable concentration gradients by leveraging the unique properties of spatially non-uniform AC electric fields. Future work will be focused on adapting this approach for generation of physiologically relevant gradients for biological research.

Acknowledgement

This work was partially supported by National Science Foundation (NSF) Division of Industrial Innovation and Partnerships IIP 1417187, IIP 1632678, and IIP 1414331. This work was also supported by teaching assistantships from the Department of Chemical Engineering at

449 Michigan Technological University.

450 **Data Availability**

451 The data that support the findings of this study are available on request from the corresponding
452 author.

453 **Conflict of Interest Statement**

454 The authors were concurrently affiliated with MicroDevice Engineering Inc
455 (microengineering.com), a spinoff from Michigan Tech, while conducting this work. The work
456 contained herein is not directly commercialize-able and thus no conflict of interest exists in
457 making it public.

458

5. References

1. Berthier, E. and D.J. Beebe, *Gradient generation platforms: new directions for an established microfluidic technology*. Lab on a chip, 2014. **14**(17): p. 3241-3247.
2. Jayaraman, S. and A.C. Hillier, *Construction and Reactivity Screening of a Surface Composition Gradient for Combinatorial Discovery of Electro-Oxidation Catalysts*. Journal of Combinatorial Chemistry, 2004. **6**(1): p. 27-31.
3. Kim, S., H.J. Kim, and N.L. Jeon, *Biological applications of microfluidic gradient devices*. Integr Biol (Camb), 2010. **2**(11-12): p. 584-603.
4. Maier, W.F., K. Stöwe, and S. Sieg, *Combinatorial and high-throughput materials science*. Angew Chem Int Ed Engl, 2007. **46**(32): p. 6016-67.
5. Potyrailo, R.A. and V.M. Mirsky, *Combinatorial and High-Throughput Development of Sensing Materials: The First 10 Years*. Chemical Reviews, 2008. **108**(2): p. 770-813.
6. Sackmann, E.K., A.L. Fulton, and D.J. Beebe, *The present and future role of microfluidics in biomedical research*. Nature, 2014. **507**(7491): p. 181-9.
7. Markevich, N.I., et al., *Long-range signaling by phosphoprotein waves arising from bistability in protein kinase cascades*. Mol Syst Biol, 2006. **2**: p. 61.
8. Kholodenko, B.N., J.F. Hancock, and W. Kolch, *Signalling ballet in space and time*. Nature Reviews Molecular Cell Biology, 2010. **11**(6): p. 414-426.
9. Fuller, B.G., et al., *Midzone activation of aurora B in anaphase produces an intracellular phosphorylation gradient*. Nature, 2008. **453**(7198): p. 1132-1136.
10. Van Haastert, P.J. and P.N. Devreotes, *Chemotaxis: signalling the way forward*. Nat Rev Mol Cell Biol, 2004. **5**(8): p. 626-34.
11. Weber, M., et al., *Interstitial dendritic cell guidance by haptotactic chemokine gradients*. Science, 2013. **339**(6117): p. 328-32.
12. Ichimura, K., S.-K. Oh, and M. Nakagawa, *Light-Driven Motion of Liquids on a Photoresponsive Surface*. Science, 2000. **288**(5471): p. 1624.
13. Daniel, S., M.K. Chaudhury, and J.C. Chen, *Fast Drop Movements Resulting from the Phase Change on a Gradient Surface*. Science, 2001. **291**(5504): p. 633.
14. Morgenthaler, S., C. Zink, and N.D. Spencer, *Surface-chemical and -morphological gradients*. Soft Matter, 2008. **4**(3): p. 419-434.
15. Lin, X., Q. He, and J. Li, *Complex polymer brush gradients based on nanolithography and surface-initiated polymerization*. Chemical Society Reviews, 2012. **41**(9): p. 3584-3593.
16. Jeon, N.L., et al., *Generation of Solution and Surface Gradients Using Microfluidic Systems*. Langmuir, 2000. **16**(22): p. 8311-8316.
17. Kim, S., H.J. Kim, and N.L. Jeon, *Biological applications of microfluidic gradient devices*. Integrative Biology, 2010. **2**(11-12): p. 584-603.
18. Keenan, T.M. and A. Folch, *Biomolecular gradients in cell culture systems*. Lab on a Chip, 2008. **8**(1): p. 34-57.
19. Krabbenborg, S.O. and J. Huskens, *Electrochemically Generated Gradients*. Angewandte Chemie International Edition, 2014. **53**(35): p. 9152-9167.
20. Faulkner, A.J.B.L.R., *Electrochemical Methods: Fundamentals and Applications 2nd Edition*. 2000.
21. Ashraf, K.M., et al., *On the Importance of Silane Infusion Order on the Microscopic and*

502 *Macroscopic Properties of Multifunctional Charge Gradients*. ACS Omega, 2020. **5**(34): p.
503 21897-21905.

504 22. Ratcliff, E.L. and A.C. Hillier, *Directed Electrodeposition of Polymer Films Using Spatially*
505 *Controllable Electric Field Gradients*. Langmuir, 2007. **23**(19): p. 9905-9910.

506 23. Hakimian, A., S. McWilliams, and A. Ignaszak, *ZnO Synthesized Using Bipolar Electrochemistry:*
507 *Structure and Activity*. Materials (Basel), 2019. **12**(3).

508 24. Hansen, T.S., et al., *Complex Surface Concentration Gradients by Stenciled "Electro Click*
509 *Chemistry"*. Langmuir, 2010. **26**(20): p. 16171-16177.

510 25. Dillmore, W.S., M.N. Yousaf, and M. Mrksich, *A Photochemical Method for Patterning the*
511 *Immobilization of Ligands and Cells to Self-Assembled Monolayers*. Langmuir, 2004. **20**(17): p.
512 7223-7231.

513 26. Carreón-González, C.E., et al., *Electrodeposition Growth of Nanowire Arrays with Height*
514 *Gradient Profiles for Microwave Device Applications*. Nano Letters, 2011. **11**(5): p. 2023-2027.

515 27. Tschulik, K., et al., *Effects of well-defined magnetic field gradients on the electrodeposition of*
516 *copper and bismuth*. Electrochemistry Communications, 2009. **11**(11): p. 2241-2244.

517 28. Ferrin, P., et al., *Reactivity descriptors for direct methanol fuel cell anode catalysts*. Surface
518 Science, 2008. **602**(21): p. 3424-3431.

519 29. Collins, J.L., et al., *Electrical and chemical characterizations of hafnium (IV) oxide films for*
520 *biological lab-on-a-chip devices*. Thin Solid Films, 2018. **662**: p. 60-69.

521 30. Toh, A.G.G., et al., *Engineering microfluidic concentration gradient generators for biological*
522 *applications*. Microfluidics and Nanofluidics, 2014. **16**(1-2): p. 1-18.

523 31. Yota, J., H. Shen, and R. Ramanathan, *Characterization of atomic layer deposition HfO₂,*
524 *Al₂O₃, and plasma-enhanced chemical vapor deposition Si₃N₄ as metal-insulator-metal*
525 *capacitor dielectric for GaAs HBT technology*. Journal of Vacuum Science & Technology A,
526 2013. **31**(1).

527 32. S. Habibi, H.Y.L., H. Moncada-Hernandez, A.R. Minerick, *Induction and Suppression of Cell*
528 *Lysis in an Electrokinetic Microfluidic System*. Electrophoresis, 2021. **accepted pending minor**
529 **revisions**.

530 33. Xie, C.G., J. Bostaph, and J. Pavio, *Development of a 2 W direct methanol fuel cell power*
531 *source*. Journal of Power Sources, 2004. **136**(1): p. 55-65.

532 34. Bazant, M.Z., K. Thornton, and A. Ajdari, *Diffuse-charge dynamics in electrochemical systems*.
533 Physical Review E, 2004. **70**(2).

534 35. Rani, S.A., B. Pitts, and P.S. Stewart, *Rapid diffusion of fluorescent tracers into Staphylococcus*
535 *epidermidis biofilms visualized by time lapse microscopy*. Antimicrobial Agents and
536 Chemotherapy, 2005. **49**(2): p. 728-732.

537 36. Galambos, P. and F.K. Forster. *Micro-Fluidic Diffusion Coefficient Measurement*. 1998.
538 Dordrecht: Springer Netherlands.

539 37. Hawlicka, E. and D. Swiatla-Wojcik, *Dynamic properties of the NaCl-methanol-water systems -*
540 *MD simulation studies*. Physical Chemistry Chemical Physics, 2000. **2**(14): p. 3175-3180.

541 38. Mohsen-Nia, M., H. Amiri, and B. Jazi, *Dielectric Constants of Water, Methanol, Ethanol,*
542 *Butanol and Acetone: Measurement and Computational Study*. Journal of Solution Chemistry,
543 2010. **39**(5): p. 701-708.

544 39. An, R., et al., *Solution pH change in non-uniform alternating current electric fields at*
545 *frequencies above the electrode charging frequency*. Biomicrofluidics, 2014. **8**(6): p. 064126.

- 546 40. Chenyakin, Y., *Are diffusion coefficients calculated using the Stokes-Einstein equation*
547 *combined with viscosities consistent with measured diffusion coefficients of tracer organics*
548 *within organics-water mediums?* 2015.
- 549 41. Persat, A., R.D. Chambers, and J.G. Santiago, *Basic principles of electrolyte chemistry for*
550 *microfluidic electrokinetics. Part I: Acid-base equilibria and pH buffers.* Lab on a Chip, 2009.
551 **9**(17): p. 2437-2453.
- 552 42. Persat, A., M.E. Suss, and J.G. Santiago, *Basic principles of electrolyte chemistry for*
553 *microfluidic electrokinetics. Part II: Coupling between ion mobility, electrolysis, and acid-base*
554 *equilibria.* Lab on a Chip, 2009. **9**(17): p. 2454-2469.
- 555 43. Ramos, A., et al., *AC Electric-Field-Induced Fluid Flow in Microelectrodes.* J Colloid Interface
556 Sci, 1999. **217**(2): p. 420-422.
- 557 44. Moreau, D., et al., *Rhodamine B as an optical thermometer in cells focally exposed to infrared*
558 *laser light or nanosecond pulsed electric fields.* Biomed Opt Express, 2015. **6**(10): p. 4105-17.
- 559 45. Bockris, J.O.M., et al., *Modern Electrochemistry.* 2000: Springer.
- 560 46. Jackson, M.J., *Microfabrication and Nanomanufacturing.* 2005: Taylor & Francis.
- 561 47. Alijó, P.H.R., et al., *Effects of electrostatic correlations on ion dynamics in alternating current*
562 *voltages.* Electrochimica Acta, 2015. **152**: p. 84-92.
- 563 48. Srivastava, S.K., et al., *Dielectrophoretic characterization of erythrocytes: Positive ABO blood*
564 *types.* ELECTROPHORESIS, 2008. **29**(24): p. 5033-5046.
- 565 49. Ramos, A., et al., *Ac electrokinetics: a review of forces in microelectrode structures.* Journal of
566 Physics D-Applied Physics, 1998. **31**(18): p. 2338-2353.
- 567 50. An, R., et al., *Solution pH change in non-uniform alternating current electric fields at*
568 *frequencies above the electrode charging frequency.* Biomicrofluidics, 2014. **8**(6): p. 13.
- 569 51. Golovnev, A. and S. Trimper, *Analytical solution of the PNP equations at AC applied voltage.*
570 Physics Letters A, 2012. **376**(16): p. 1391-1395.

572

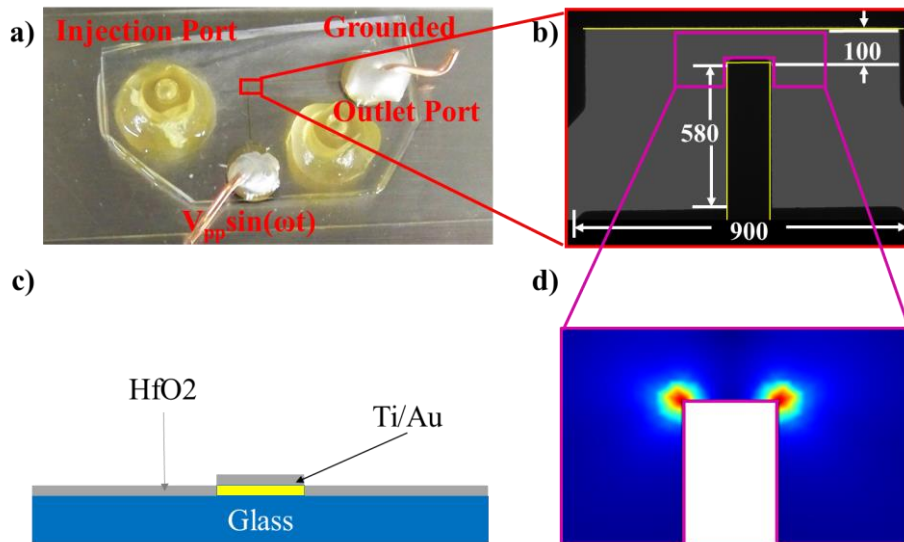


Figure 1: Microdevice design. a): Photo of device. with fluid channel filled with green dye, red box indicates the working fluidic chamber and b): Red box area under 10x microscope, c): Side view of the device. Units for d): COMSOL simulation of the gradient of electric field in labeled area in figure 1b. All numbers are micrometers.

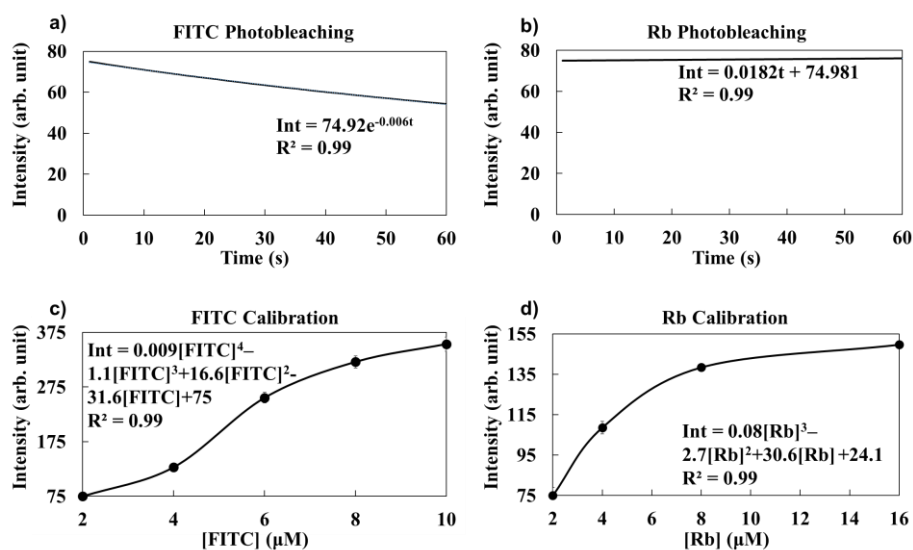


Figure 2: Dye properties study. a): Photobleaching property for FITC; b) Photobleaching property in for Rb; c) FITC emission intensity calibrated with FITC concentration and d) Rb emission intensity calibrated with Rb concentration (n = 3 for all curves)

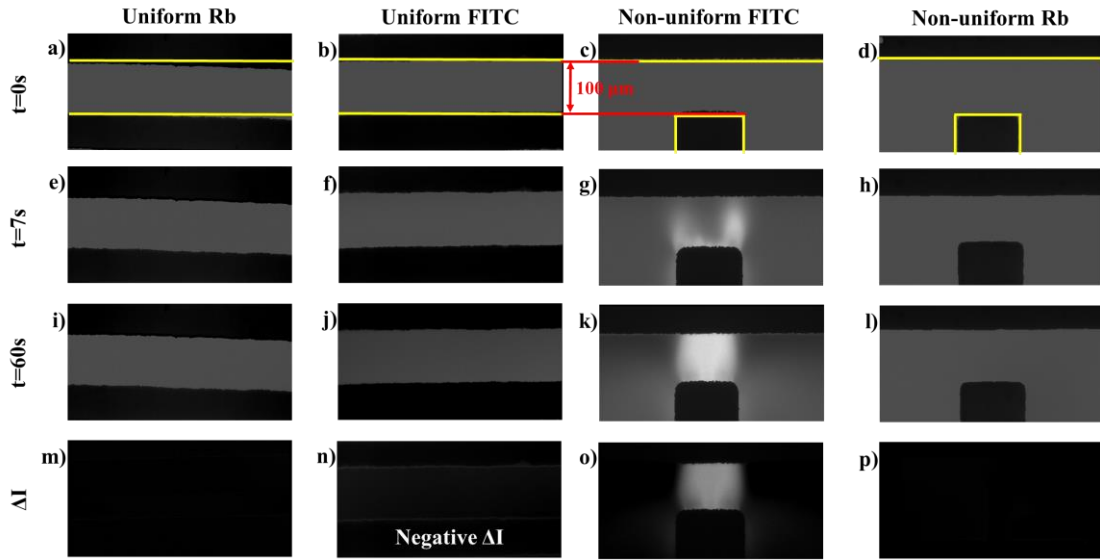


Figure 3: Comparison experiments under 100 Hz, 10V_{pp}; First column are t=0, 7, 60s and FITC intensity difference obtained by MATLAB image analysis of experiments under uniform electric field; Second column are same time and image output of Rb intensity; Third column are same time and image output of experiments under nonuniform electric field for ionized FITC; Fourth column are same information of experiments using non-ionized Rb dye in non-uniform electric field It can be observed that intensity increase can be observed in o) while no change observed m) n) and p)

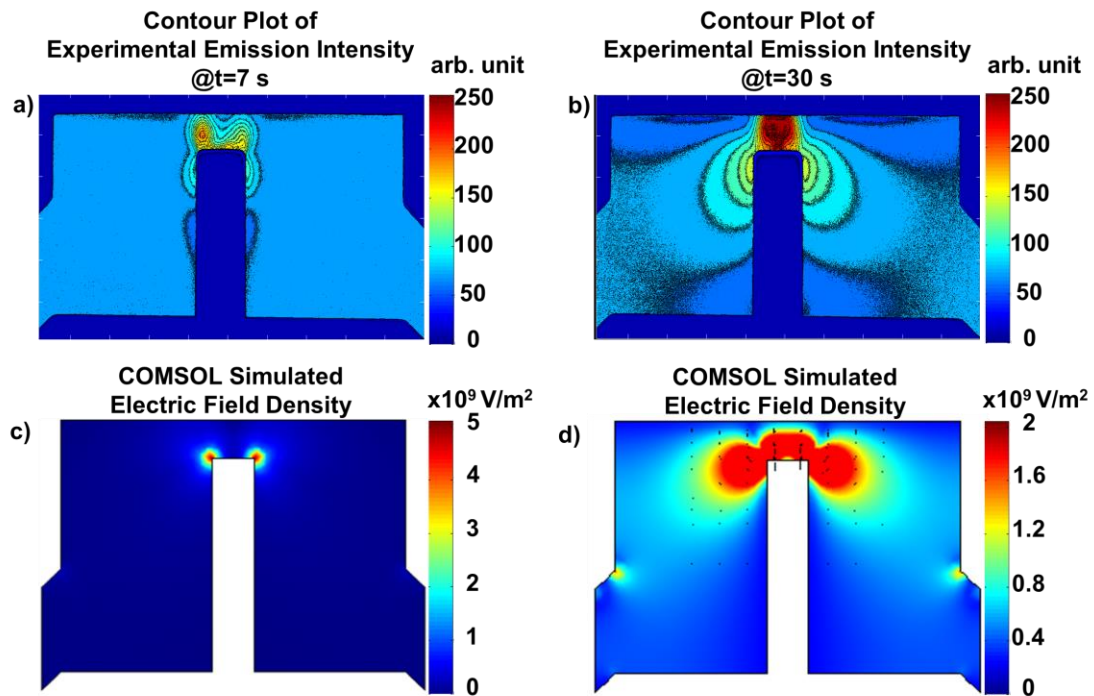


Figure 4: Spatial FITC emission intensities at $t = 7$ s (a) and $t = 30$ s (b) demonstrated similarity to the spatial distribution of electric field density (c, d). Both (c) and (d) contain the same group of data, while (c) shows the field density on a scale from 1×10^9 to 5×10^9 , and (d) shows data in the scale of 0.4×10^9 to 2×10^9 from for the purpose of visualization. These results indicate that the FITC ion concentration enriched from the highest field density area then expanded down the electric field gradient with lower concentrations in the peripheral areas.

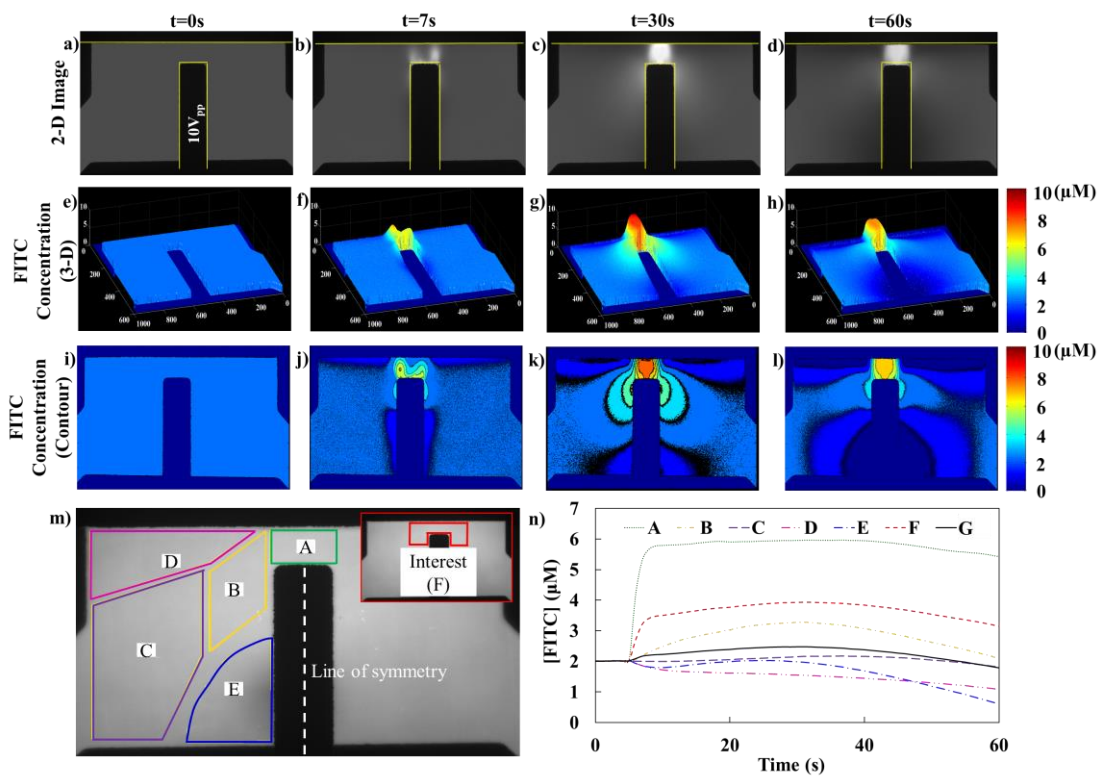


Figure 5: a)-d): Gray-scale 2-D FITC intensity plot obtained from MATLAB image analysis at $t=0, 7, 30$ and $60s$ under $10V_{pp}$ 100 Hz; e)-h): 3-D MATLAB plot at same time point and i)-l): Matlab contour plot showing the FITC intensity gradient. Yellow box in figure m) shows the position of sampled intensity. Figure n) is showing the time dependency of the average of sampled intensity.

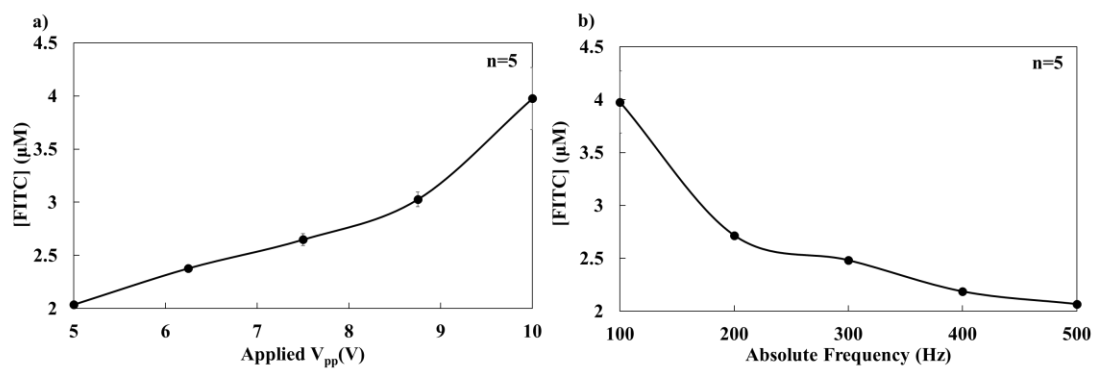


Figure 6: a) : potential dependency (5 to 10 V_{pp}) of FITC concentration at 100 Hz and b): frequency dependency (100 to 500 Hz, 5 to 25 times electrode charging frequency) of FITC concentration at 10 V_{pp} . FITC concentration change increased with peak-to-peak potential and decreased with frequency.